OTC 2024

OTC-35402-MS

Process-Oriented Validation of HYCOM-TSIS Reanalysis Runs for the Northern Gulf of Mexico

L. Ivanov[1], R. Arena[1], A. Bozec[2], E. Chassignet[2], S. Longridge[1], R. Ramos[1], A. Srinivasan[3], M. Iskandarani[4]

[1]Woods Hole Group, Inc., Bourne, MA, USA
[2]Florida State University, Tallahassee, FL, USA
[3]Tendral LLC, Key Biscayne, FL, USA
[4]University of Miami, Coral Gables, MA, USA

Abstract

The Tendral Statistical Interpolation (T-SIS) package is used with HYCOM to produce the reanalysis hindcast. To assess 1/25° and 1/100° resolution model hindcasts' performance, model results were compared to independent ADCP current measurements from several sites in the Northern GOM impacted by passing Loop Current Eddies, Deep Cyclonic Eddies (without a clear surface expression) and Tropical Storms. The comparative analysis of HYCOM-TSIS reanalysis data and ADCP measurements showed a good qualitative and satisfactory quantitative agreement between model and observations. Of most importance, the model with the T-SIS package resolves the general kinematic structure of subsurface flows associated with the Deep Cyclonic Eddies, reflecting a substantial improvement of the model skill compared to the previous version of the hindcast.

Introduction

The main purpose of this paper is to evaluate the performance of HYCOM-TSIS through a comparative analysis of the model reanalysis product with observations. In addition, the model output is used to detail characteristics, generation regions, and evolution of some processes in focus. The approach adopted for this analysis is to test how well the reanalysis product represents the most energetic oceanographic phenomena in the Gulf of Mexico (GOM). Three phenomena are considered: (i) strong flows associated with the Loop Current (LC) and Loop Current Eddies (LCE), (ii) subsurface flows, and (iii) flows generated by tropical storms. This paper mainly focuses on subsurface flow events, which are typically not well represented in reanalysis products from several other/older ocean circulation models for the GOM [Ivanov et al., 2018]. These events are of particular interest since the energy source does not seem to originate at the surface. Additionally, the existence of intense subsurface currents in practice requires serious attention of deepwater operators due to increased loads on offshore structures and higher risk of operations. Therefore, even the presence of subsurface flows in the model reanalysis product and a qualitative match to observations would mean a success story in regard to model performance.

The paper is organized as follows. The model details and description of the observational data used in the study are discussed in the sections following this introduction. A brief overview of the energetic phenomena is provided in Section 4. The results of the analyses are provided Section 5 and summarized in the Discussion and Summary Section.

HYCOM-TSIS

HYCOM with the Tendral Statistical Interpolation data assimilation package from the Center for Ocean-Atmospheric Prediction Studies has two versions for the Gulf of Mexico, one with a 1/100° (~1km) horizontal resolution (HYCOM-TSIS GOMb0.01) and another with a 1/25° (~4km) resolution (HYCOM-TSIS GOMb0.04). Tidal forcing is included and is described by five tidal harmonic constituents: M2, S2, O1, K1, and N2. Both versions of the model reanalysis product are available from 01/01/2001 to 12/31/2020.

The GOMb0.01 version is set-up with high resolution 1km bathymetry of the Gulf of Mexico (GRIIDC, [Velissariou, 2014] over a domain that spans from 98ºW to 77ºW in longitude and from 18ºN to 32ºN in latitude. With 41-hybrid layers in the vertical, the latest version of the HYCOM model (2.3.01: https://github.com/HYCOM/HYCOM-src) is forced at the surface with the CFSR hourly atmospheric forcing from 2001 to 2011 and CFSv2 from 2012 onward. The lateral open boundaries are relaxed to daily means of the global HYCOM GOFS3.1 reanalysis (https://www.hycom.org/dataserver/gofs-3pt1/reanalysis). The initial conditions are taken from a non-assimilative simulation with a state corresponding to January 1st, 2001. Five tidal constituents (M2, S2, O1, K1, and N2) are applied at the surface through a local tidal potential and at the boundaries with the Browning-Kreiss boundary conditions. Tidal data are extracted from Oregon State University (OSU) tidal models: the TPXO9 atlas [Egbert & Erofeeva, 2002].

The GOMb0.04 domain and simulation are based on the same bathymetry as the GOMb0.01 but interpolated on the 1/25º grid. Initial conditions, atmospheric forcing and boundary conditions are set up the same way as in the 1km domain.

The Tendral Statistical Interpolation (TSIS) package [Srinivasan et al., 2022] is used with HYCOM to produce the hindcast. The basic functionality of the package is multivariate linear statistical estimation given a predicted ocean state and observations. To optimize the system's performance for the HYCOM Lagrangian vertical coordinate system, subsurface profile observations are layerized (re-mapped onto the model hybrid isopycnic-sigma-z vertical coordinate system) prior to assimilation. The analysis procedure then updates each layer separately in a vertically decoupled manner. A layerized version of the Cooper & Haines [1996] procedure is used to adjust model layer thicknesses in the isopycnic-coordinate interior in response to sea surface height (SSH) anomaly innovations. Prior to calculating SSH innovations, the mean dynamic topography (MDT) is added back into the altimetry observations. An MDT derived from a 20-year freerun of the GOMb0.04 configuration, is used for converting sea level anomaly (SLA) to SSH. The multi-scale sequential assimilation scheme based on a simplified ensemble Kalman Filter [Evensen, 2003; Oke et al., 2002] is used to combine the observations and the model to produce best estimates of the ocean state at analysis time. This state is then inserted incrementally into HYCOM over 9 hours. The analysis is done daily at 18Z.

In the 1/100º version, since observations that are fed to the assimilation system (TSIS) are not of a high enough resolution compared to the grid resolution, the reanalysis is performed on the 1/25º grid. The GOMb0.01 ocean state is box-car averaged at 1/25º to remove the small-scale variability and given to TSIS as the ocean state. The assimilation system then performs the reanalysis at this resolution and provides an increment that is then interpolated back at 1/100º and added to the GOMb0.01 ocean state.

The TSIS assimilative system accepts SLA, sea surface temperature (SST) and temperature-salinity (T/S) profiles. For these hindcasts, we assimilate remotely sensed SLA and SST as well as *in-situ* T/S considered to be the most reliable observations. Along-track SLA from four operational satellite altimeters (T/P, Jason 1,2, Envisat, GFO and Cryosat) constitute the most important data set for constraining the model. The data are available from Collecte Localisation Satellites (CLS) from January 1993 to present. These data are geophysically corrected for tides, inverse barometer, tropospheric, and ionospheric signals [Dorandeu & Le Traon, 1998; Le Traon & Ogor, 1998]. For the sea surface temperature, we use the SST (Foundation Temperature) Level 4 product from NAVOCEANO (GHRSST) and NOAA/NODC (AVHRR) which integrates several individual sensors and provides a gridded field with error estimates. ARGO drifters are also used to constrain the sub-surface density structure when available over the hindcast period.

Model outputs include the profiles of the three current velocity components and of water temperature and salinity, as well as sea surface height, thickness of the upper mixed layer, and barotropic flow velocity.

Observational Data

NTL Dataset.

Current time-series used for direct comparison with the model hindcast data were obtained from measurements collected as part of the Bureau of Ocean Energy Management, Regulation, and Enforcement (BOEMRE) Notice to Lessees (NTL) program in the GOM. First compelled by a 2005 (BOEMRE Notice to Lessees (NTL) mandate, operators drilling in water depths deeper than 400 meters in the GOM are required to collect current profile measurements within the upper 1,000 meters of the water column and to measure near bottom currents when drilling nearby the Sigsbee Escarpment.

ADCP measurements collected as part of the NTL program are measured from floating production facilities (FPFs) and mobile offshore drilling units (MODUs). Such data are collected primarily using Teledyne RD Instruments (TRDI) ADCPs mounted on the platform/rig itself or on nearby moorings. Oil platforms and rigs are inherently difficult environments to collect accurate current data due to a variety of factors, which include noise from drilling activities, potential interference with the flow by the structures, and possible acoustic interference from the risers, flowlines, remotely operated vehicles and other physical elements. Therefore, the ADCP records used in this study had been subjected to rigorous quality control procedures by Woods Hole Group (WHG) oceanographers in the framework of projects funded by industry and the National Academy of Science, Engineering, and Medicine (NASEM) – Understanding Gulf Ocean Systems (UGOS) program.

Frontal Delineation Dataset.

To put the occurrence of each strong mid-water flow event into oceanographic context, results from the manual frontal delineation analyses conducted by the Woods Hole Group team that are produced daily for the Oil Industry operators in the GOM were used [Storie et al., 2023]. These analyses are performed using various data sources, such as satellite imagery, drifters, ADCP transect data, point ADCP observations, and hydrodynamic models.

The field measurements (ADCP and drifter data) are used to determine the precise location of the 1.5-knot velocity, typically coinciding with the frontal edge. Thus, the resulting delineated front is a proxy for the 1.5-knot velocity magnitude value. Frontal positions are adjusted based on thermal and chlorophyll gradients observed in SST and ocean color imagery. The trajectories of the surface drifters,

strategically deployed by WHG, are the primary data source used for defining the northern extent and strength of the LC, tracking both named eddies (that shed from the LC) and the smaller scale frontal cyclonic eddies (CEs), and monitoring the currents associated with these features as they migrate through the GOM. Direct measurements of surface current velocities allow for the most accurate placement of the 1.5-knot velocity gradient in the local area. Next, Rig-ADCP data is considered with the assumption that surface currents are equal to or greater than the measurement at the ADCP first bin depth (typically between 40 to 80 meters water depth). Global and regional forecast model nowcasts are referenced at the final step of this process, particularly for areas with limited data coverage and/or excessive cloud coverage. The systematic frontal analysis described results in a unique long-term continuous oceanographic dataset that was used in this study to better understand details of the GOM near-surface circulation patterns during events under consideration.

Oceanographic Features/Processes in Focus

Subsurface Flows.

The occurrence, possible mechanisms, and some features of strong currents characterized by a subsurface intensification that does not have a clear expression at the surface were the subjects of a study conducted by the Minerals Management Service (MMS which is now BOEM) [DiMarco et al., 2004]. The authors described such phenomenon as 'subsurface jets' and established the following definition. Mid-water jets are flows that typically have temporal durations of a few hours to one day, have subsurface speed maxima that can exceed 2m/s, have peak speeds that occur between 150-350m below the sea surface, and have little or no energetic surface expression. It is hypothesized that subsurface jets could be caused by the interaction of the LC with bottom topography and/or eddy-eddy interaction. Based on ADCP records collected over a twelve-year period (1990-2001), DiMarco et al. [2004] identified a total of 13 subsurface jet events. Ten more similar events were identified and described by Hamilton & Badan [2009]. Although in the latter study, the authors use the same term 'jet', the description of the events is substantially different from the events described in the initial study by DiMarco et al. [2004]. In particular, none of the ten events in Hamilton and Badan [2009] had current speed in excess of 0.75m/s, and the event duration varied between 1 and 8 days. Hamilton and Badan found subsurface jet events to be fairly rare events (10 events in 18 years of ADCP measurements) and that regions where strong eddy fields can interact with continental slope topography were favorable conditions for jets to appear. Events found in the more recent measurements [Ivanov et al., 2018; Magnell & Ivanov, 2014], in terms of their characteristics, were similar to the events described in Hamilton and Badan's study.

Based on the 2005-2010 NTL data, in approximately 70 cases, the events of mid-water flows were characterized by current maxima in the range of 0.4-0.6m/s that were located between 300m and 800m, most frequently around 500m [Magnell and Ivanov, 2014], much deeper than the 150-350m depth range identified in DiMarco et al. [2004]. Some of these 70 events identified lasted for less than one day, but unlike the 'jet' flows identified in DiMarco et al. [2004], many events identified in the NTL data were of a significantly longer duration. Since the maximum subsurface current speed did not exceed 0.7m/s in all recent cases, we define the term subsurface 'flow' (not a jet) as currents that occur at depths between 100m and 800m, that last for more than a day, have a velocity maximum over 0.3m/s, and are topped by much weaker near-surface currents. Analysis of the 2011-2020 NTL data, that was performed for the comparison with HYCOM_TSIS, identified 29 subsurface flow events for further investigation (Table 1).

Loop Current and Loop Current Eddies.

The LC system dominates the dynamics and mesoscale variability of ocean currents throughout the deep GOM. The LC is formed as water from the Caribbean Sea enters the southeastern Gulf via the Yucatan Strait, flows northward, loops eastward and then southward, and finally exits as the Florida Current between Key West and Cuba [[Hamilton, 1990]. This flow becomes this Gulf Stream as it turns northward around the Florida peninsula and continues along the eastern U.S. seaboard and across the northern Atlantic Ocean. The LC generally occupies the central and eastern Gulf; however, the feature routinely penetrates well into the northern Gulf (as far north as 29°00'N) and occasionally develops a westward extension reaching as far west as 94°00'W. As the LC penetrates north into the GOM, the southern portion of its structure narrows, bringing the eastern and western fronts closer to each other. An internal closed circulation develops within the northern portion and pinches off a large (radius ~100 to 300km) anticyclonic LCE. The shedding and migration of LCEs is facilitated and affected by the presence and movement of frontal cold-core cyclonic eddies (CEs) [Vukovich & Maul, 1985]. LC shedding dynamics do not have a specific periodicity or seasonality, though LCEs form and separate at intervals from 3 to 18 months and multiple eddies can exist in the GOM at a given time [Lewis et al., 1989]. The LC typically retreats southward following eddy separation. Eddies migrate either northward, northwestward, or westward at speeds typically averaging 5km to 8km per day while also rotating clockwise [Vukovich & Crissman, 1986]. The rates of migration and rotation depend heavily on the size, depth, and location of the eddy in addition to outside influences such as topography, frontal CEs, and continued interactions with the LC. Ultimately, LCEs migrate southwestward toward the western boundary of the Gulf where they gradually decrease in size and strength [Vukovich & Maul, 1985]. The typical lifespan of a LCE is one year [Vukovich & Crissman, 1986].

Table 1. Records containing observations of sub-surface flows derived from the analyses of the 2011-2020 NTL ADCP data and used for comparison with HYCOM-TSIS hindcast data.

Station ID	Latitude, Longitude (deg)	Time of sub-surface flow event occurrence	Current speed, m/s	Flow direction
42364	29.05N, 88.08W	End of December 2010	0.65	E
42364	29.05N, 88.08W	August 2010	0.5	E, SW
42369	27.19N, 90.27W	October 2016	0.7	S, NE
42374	28.86N, 88.05W	16-25 March 2011.	0.65	S, NW
42374	28.86N, 88.05W	September 2013.	0.65	N-NE
42377	27.29N, 90.96W	August 2012	0.5	SW
42390	26.12N, 94.89W	2-10 May 2020	0.6	N
42390	26.12N, 94.89W	1-10 September 2020	0.65	SW
42862	27.57M, 92.39W	1-5 May 2014	0.4	SW
42864	28.47N, 88.09W	October - November 2019	0.45	SW
42864	26.31N, 94.40W	September - October 2020	0.55	SW-W
42865	27.08N, 90.79W	Mid-May 2016	0.4	SE-E
42865	27.41N, 90.26W	October 2016	0.6	SW-W
42874	27.52N, 90.16W	5-15 October 2018	0.5	W
42876	26.20N, 91.44W	Mid-June 2019	0.5	W
42882	28.18N, 89.13W	12-25 November 2020	0.55	SE, SW
42884	27.39N, 94.47W	2-9 March 2020	0.6	SW
42893	27.15N, 90.32W	Early May 2016	0.35	SW, NE
42898	27.02N, 92.23W	November-December 2016	0.6	W-NW
42902	28.60N, 87.97W	Multiple events	0.55	SE
42903	26.73N, 90.49W	Early April 2020	0.6	W
42914	26.00N, 91.87W	Mid-September 2011	0.6	SE
42919	28.24N, 88.92W	Mid-September 2013	0.4	E, W
42922	28.45N, 87.90W	Mid-September 2013	0.45	SE
42924	85.03N, 27.46W	Early May 2014.	0.45	SW
42925	26.73N, 90.49W	June 2012	0.5	N
42926	26.93N, 90.51W	Mid-May & Mid-June 2011	0.55	E,W; N
42931	26.10N, 92.04W	5-9 September 2014	0.35	NW, SW
42932	27.30N, 90.09W	End of April 2016.	0.5	W

Maximum current velocities within a LCE are usually observed near or at the sea surface, although there can be considerable subsurface flows as well. The LC and LCEs can generate surface currents upwards of 2.5m/s in the eastern and central Gulf, typically subsiding to slightly weaker peak speeds in the western Gulf. Moderate currents (1.0m/s) can extend to depths of ~800m [Vukovich & Crissman, 1986]. Current speeds increase monotonically inside the front (defined by the 0.75m/s velocity gradient) then decrease toward the center of circulation. Current levels drop off almost exponentially outside the front. Current velocities at a particular site in the GOM during these events largely depend on the configuration and unique path of the LCE.

Table 2. Sample records containing observations of strong surface flows associated with LC and LCE, derived from the analyses of the 2011 -2020 NTL ADCP data and frontal analysis data.

NDBC/WMO PLATFORM ID	LATITUDE, LONGITUDE (DEG)	RECORD START DATE (YYMMDD)-END DATE (YYMMDD)	Feature from Frontal Analysis
42865	27.08N, 90.79W	160512-160826	Eddy Poseidon
42377	27.29N, 90.96W	110106-120106	Galileo, Hadal, Loop Current
42925	26.73N, 90.49W	110827-120825	Icarus, Jumbo, Hadal, Loop Current, West Florida Shelf Eddies
42374	26.86N, 88.05W	101231-110924	Hadal, Franklin, Loop Current
42369	27.21N, 90.28W	130501-230501	(Mad Dog Site) Various over a 10-year period

Response to Tropical Storms.

Tropical storms/Hurricanes are phenomenon that frequently occur in the GOM. For a site located in the central northern GOM, according to historical records [Schreck & NCAR Staff (Eds.), 2022],approximately 100 tropical storms have passed within 100km from that site from 1853 to 2023. To compare model hindcast data with observations, we used data from station ID 42369 (Mad Dog) spanning periods of Hurricane Barry and Hurricane Laura.

Analysis Results

Subsurface Flows.

a) Subsurface Flow Occurrence Statistics.

From the analysis of NTL data spanning the period from 2011 to 2020, we identified a total of 29 cases that fall into the category of subsurface flow events. A map showing all locations where such events were observed over a period from 2005 to 2020 is shown in Figure 1. Although most of the dots in the map are clustered in two areas, the Mississippi and De Soto Canyons (highest spatial density) and Green Canyon, we believe this distribution is more a reflection of the spatial density of measurements rather than the density of event occurrence. At least, the gap in the density of event occurrence between the two areas, most likely, is not that obvious. The colors of the dots indicate the months in which the events occur and suggest that subsurface flow events occur more frequently during winter and spring (January- April), although a substantial number of the events occurred during September and October.

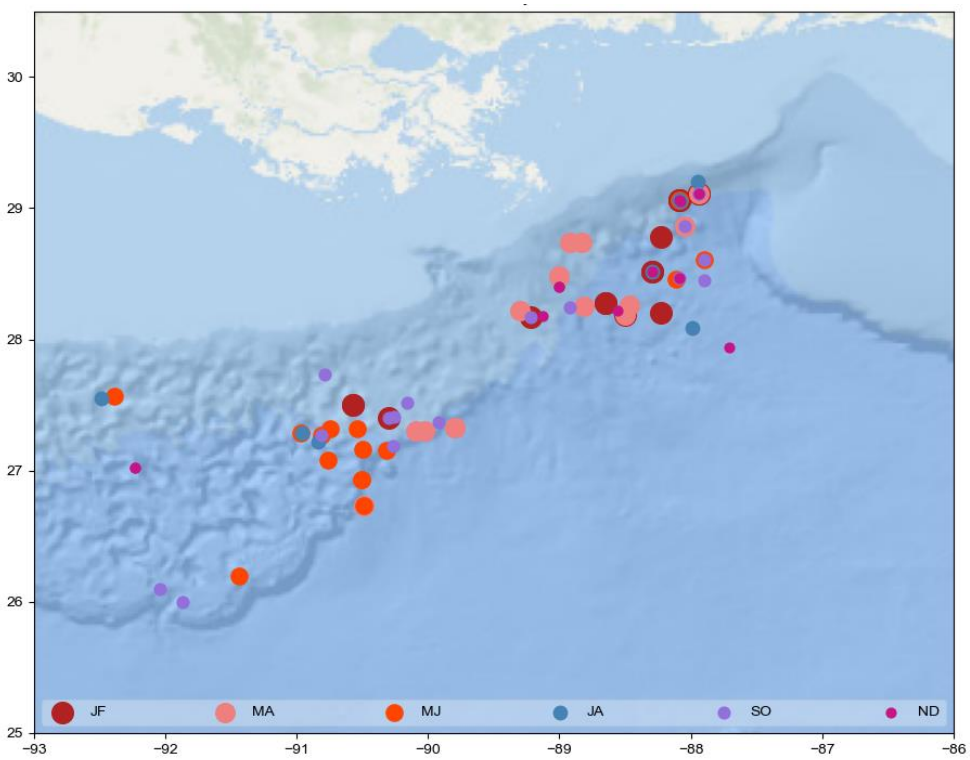

Figure 1. A map of the northern central GOM showing bottom bathymetry along with the location of the sites where the subsurface flows were observed. The months of event occurrence is defined by the color of the dots. The size of the dots varies for illustration purposes only.

b) Kinematic Structure.

The kinematic structure of a typical subsurface flow is illustrated by Figure 2. The event is characterized by two cores of elevated flow speed in the depth range from approximately 100m to 600m. Maximum speed (0.73m/s) was observed at 150m. During the event, the strong subsurface flow was going towards the south and then shifted towards the northeast and north. To emphasize the relative significance of the event in regard to flow intensity, we show the maximum flow speed profile (in red) against the average of nine maximum current speed profiles associated with nine LCE's observed at the same location (in blue) in Figure 2. That figure reveals that the maximum current speed associated with the subsurface flow events was greater than the mean profile of the maximum current speed profiles associated with LCE's below a depth of approximately 220m.

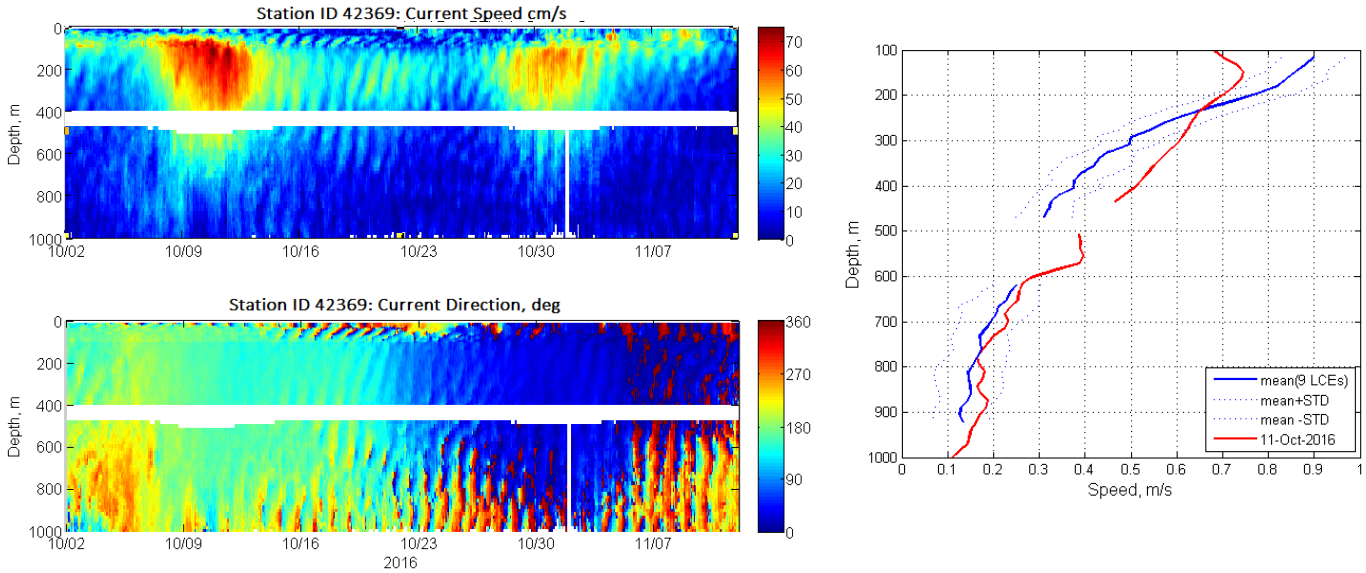

Figure 2. Time-series of current speed (left, upper) and direction (left, low) collected at station ID 42369 (Mad Dog) in October 2016 and the maximum current speed profile associated with the event shown in the left panel (red) referenced to the averaged maximum current speed profiles associated with nine (9) LCE's observed at the same location (blue).

c) Model Output vs Observations (Case Studies).

The methods of the comparative analysis of model data and observations included:

- Visual 'point-to-point' comparisons using color-filled time-series plots of current speed and direction,
- Cross-correlation analysis,
- Current speed scatter plots,
- EOF analysis of the current speed time-series,
- Wavelet analysis for inertial oscillations,
- Willmott's refined index of model performance,
- Bulk statistics for selected depths, including vector-averaged current speed and direction, mean and maximum current speed, direction of maximum current speed, and the time of occurrence of the maximum speed.

The visual 'point-to-point' comparisons turned out to be the most effective in terms of qualitative assessment of the accuracy of model hindcasts. In most cases, analysis of the various quantitative metrics used for data comparison is inconclusive as some metrics compared satisfactory while other metrics did not agree at all. For subsurface flow events model output agreed with observation qualitatively in approximately 40% of all considered cases.

Time-series of current speed and direction profiles from measurements and model reanalysis, for example events for which there is a qualitative agreement between model and observations, are shown in Figures 3a-c. For all these events, flow direction from the model is in satisfactory agreement with flow direction from observations, while correlation for the current speed is low. However, it is important to emphasize that reanalysis data do show subsurface flow intensification within the period of an event defined in measurement data. For example, model reanalysis data show multiple cases of subsurface flows for the period covered by the station ID 42364 measurement data (Figure 3a), also showing multiple cases of subsurface flows, although the number of cases is different for the model and measurements. For the event observed from Jim Thompson (Figure 3b), the subsurface current speed maxima show up approximately at the same time in the model and measurement time-series, but the depths of the subsurface flow core is shallower in the model data compared to measurement data. For the event shown in Figure 3c, the model shows subsurface flows but not at the time these flows were observed. Also, current speeds significantly lower in the reanalysis data.

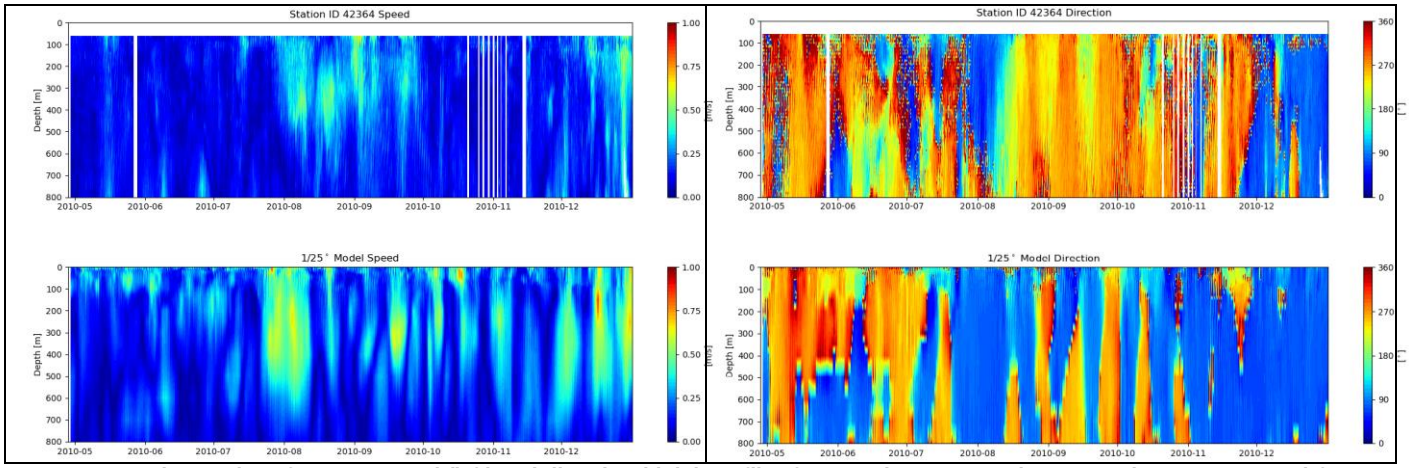

Figure 3a. Time-series of current speed (left) and direction (right) profiles from station ID 42364 (Ram Powel, 29.05N, 88.08W) for May – December 2010 (derived from observations (upper panel) and HYCOM-TSIS GOMb0.04 (lower panel).

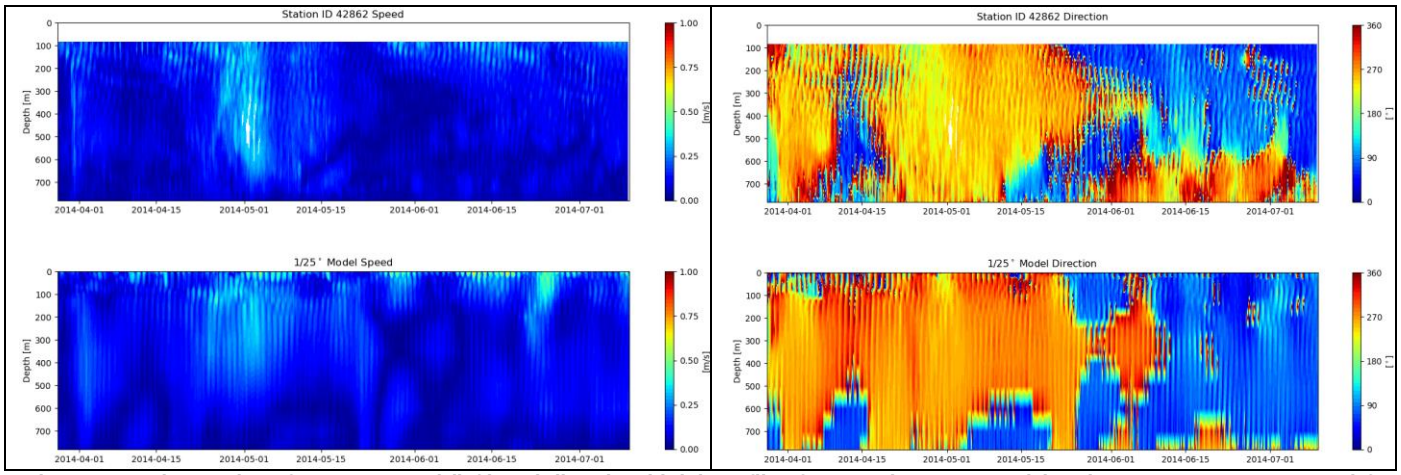

Figure 3b. Time-series of current speed (left) and direction (right) profiles from station ID 42862 (Jim Thompson, 27.57N, 92.39W) for April – June 2014 derived from observations (upper panel) and HYCOM-TSIS GOMb0.04 (lower panel).

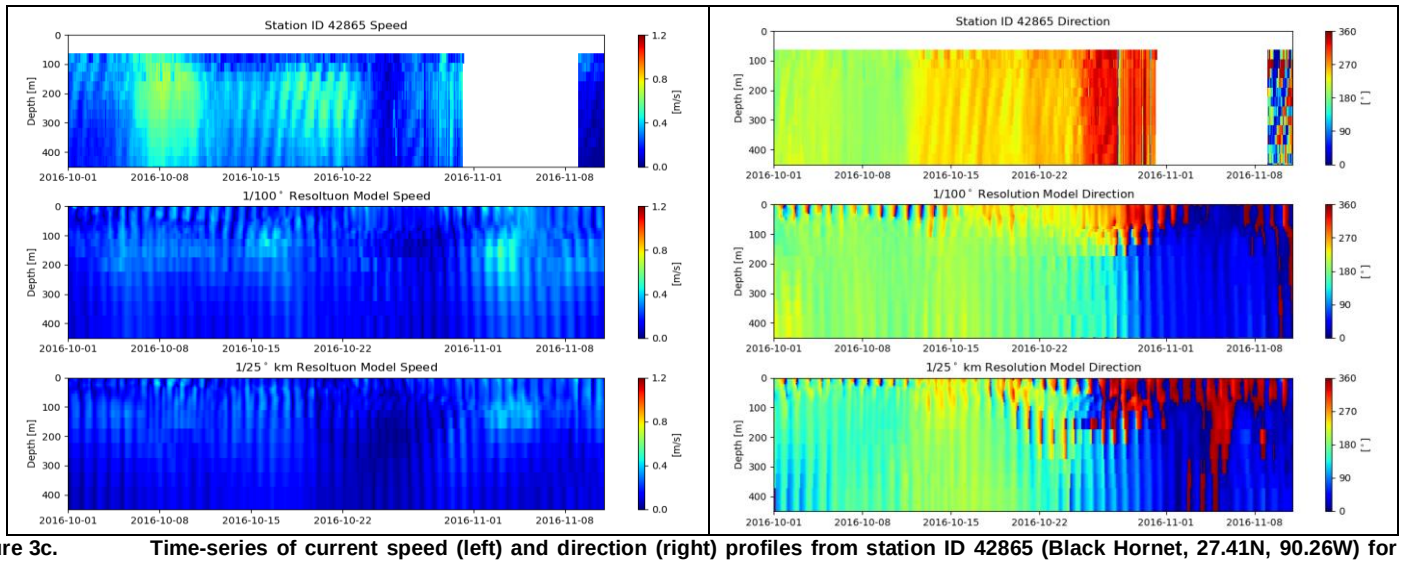

Figure 3c. Time-series of current speed (left) and direction (right) profiles from station ID 42865 (Black Hornet, 27.41N, 90.26W) for October 2016 derived from observations (upper panel), HYCOM-TSIS GOMb0.01 (middle panel), and HYCOM-TSIS GOMb0.04 (lower panel).

d) Origin and Evolution of a Subsurface Cyclonic Eddy Observed in October 2016.

Our process-oriented analysis of the combination of the model and measurement data allowed us to pinpoint the origin of the cyclonic subsurface eddy observed in at the Mad Dog site (Station ID 42369) in October 2016. In that combination, model +

measurements, the measurements played the role of the ground truth proving the eddy described by the model is not an artifact. The model data, in turn, allowed us to trace the eddy evolution over a period of several months, illustrated in Figure 4.

In March of 2016, a subsurface cyclonic eddy (CE) formed off of the end of the LC intrusion in the Gulf of Mexico. The northern edge of the LC extended towards the DeSoto Canyon and interfered with the western slope, causing the deeper current to be redirected toward the northwest, forming a cyclonic eddy. While this CE was forming, a larger anticyclonic LCE was also beginning to form from the LC. From March to June, the CE stayed where it formed, off of the DeSoto Canyon basin, persisting as the northeastern flow from the LC/ forming-LCE continued to run into the western slope, feeding the system. The CE had an oval shape with its longest diameter (major axis) running from southwest to northeast during this period.

By mid-June, the larger LCE separated from the LC and started to propagate west, and the deep cyclonic eddy stayed stationary and continued to exist with steady flow. As the LCE continued to travel westward in June to August, the CE started to move slightly to the northwest, becoming more circular in shape and growing larger. In September 2016, the CE was its largest size and started its propagation towards the west, reaching MD (shown in Figure 4 as a red square) by October 10th, 2016. The eddy moved most rapidly in October and had moved west, past the MD site by October 16th. The CE then began to dissipate, decreasing in size, in the central Gulf in November.

Note that the dates of the eddy fronts passing the site are (approximately) the same as derived from the measurement data. The data reveal an eddy without a surface expression, while the model represents it as a deep eddy but with a surface signature. This is the major difference in how the eddy is represented in the model compared to observations. We hypothesize that the Mississippi runoff may cause the deep circulation to be decoupled from the circulation at the surface. The phenomenon, is possibly, not entirely accounted for in the model.

The deep cyclonic eddies of the type described above are typically observed within the area of the Mississippi Delta and over the western slope of the DeSoto canyon [Ivanov et al, 2018,Magnell & Ivanov, 2014]. Oey & Zhang [2004] describe a mechanism for the generation of subsurface cyclonic eddies and jets in the area of De Soto Canyon when an energetic LCE interacts with a continental slope and shelf.

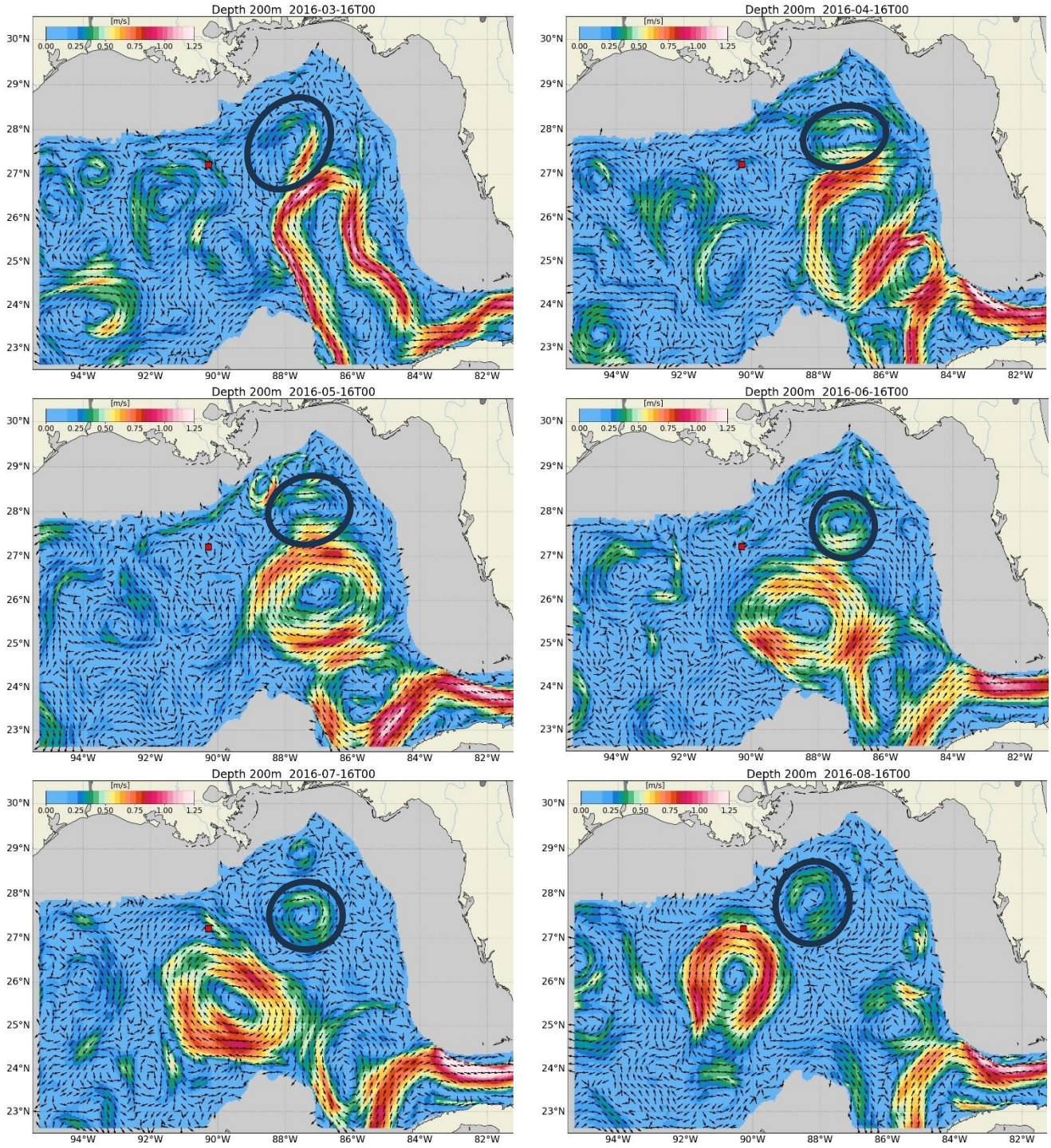

Figure 4. Current velocity maps for 200m depth covering the life cycle of the deep cyclonic eddy observed at several sites in October 2016. Mad Dog is represented as a red square. The dark blue outline is present to guide the reader's eye to the subsurface cyclonic eddy.

Loop Current and Loop Current Eddies.

As a preliminary step in the analysis, we investigated how well the model represents more prominent, energetic events, such as the LC and LCE's. The cases that were selected for that model-to-observations comparison showed good agreement between these datasets for the periods of LCE events. Current speed and direction plots for three example cases are shown in Figures 5a-c. We conclude that in all these cases the agreement between model and observations may be considered satisfactory because:

- Peak current speeds in the model and observations occur approximately at the same time,
- Peak current magnitudes in the model data set and in the observations are similar,
- Penetration of the strong currents into sub-surface layers is almost the same in model and observational data,
- The evolution of current direction is similar in model data and observations.

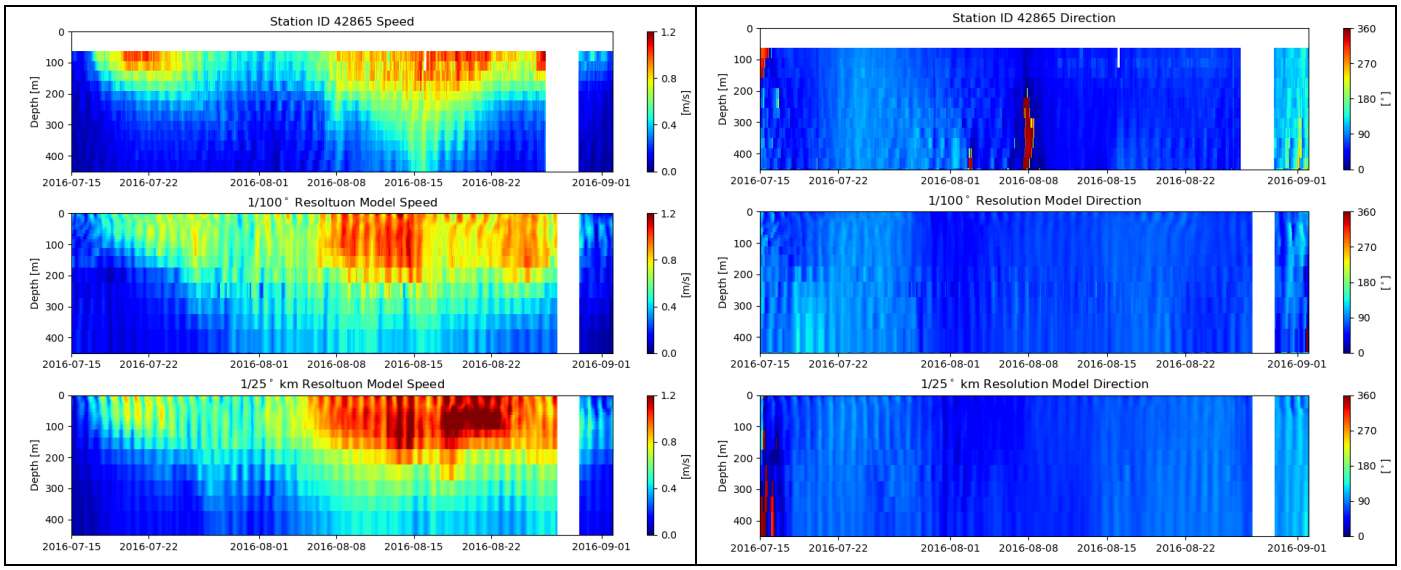

Figure 5a. Time-series of current speed (left) and direction (right) profiles from station ID 42865 (Black Hornet) derived from observations (upper panel), HYCOM-TSIS GOMb0.01 (middle panel), and HYCOM-TSIS GOMb0.04 (lower panel).

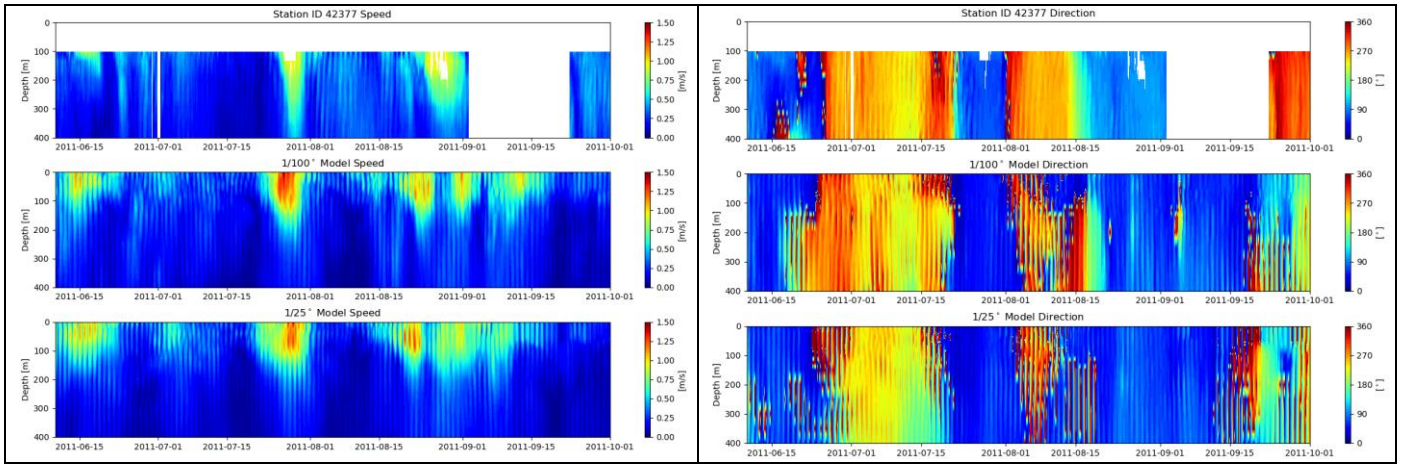

Figure 5b. Time-series of current speed (left) and direction (right) profiles from station ID 42377 (Constitution, 27.29N, 90.97W) derived from observations (upper panel), HYCOM-TSIS GOMb0.01 (middle panel), and HYCOM-TSIS GOMb0.04 (lower panel).

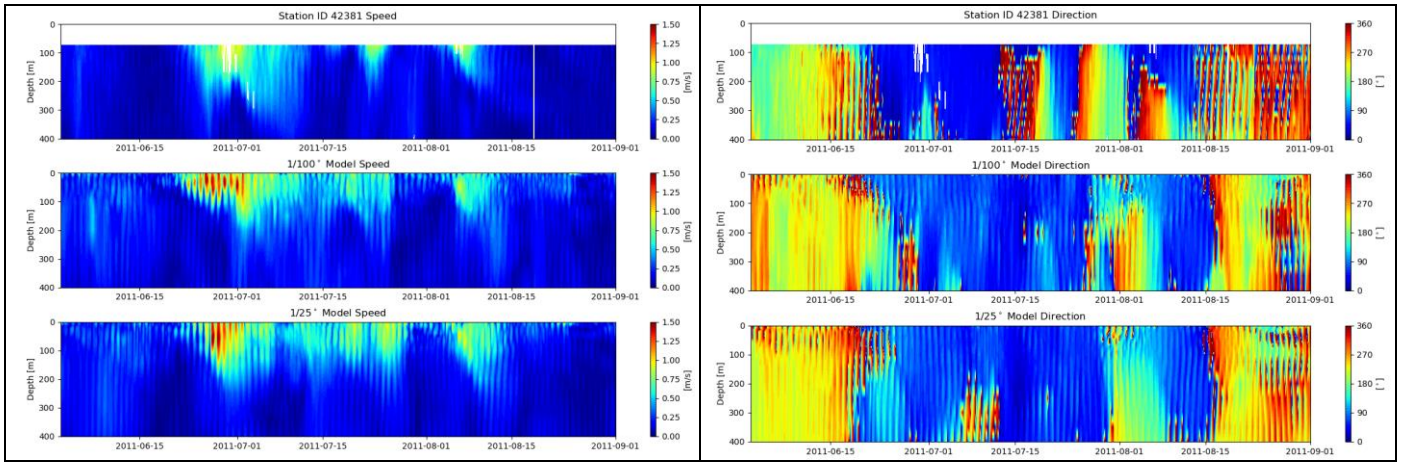

Figure 5c. Time-series of current speed (left) and direction (right) profiles from station ID 42377 (Gomez Hub, 28.22N, 89.61W) derived from observations (upper panel), HYCOM-TSIS GOMb0.01 (middle panel), and HYCOM-TSIS GOMb0.04 (lower panel).

The visual comparison of the observational data and model results, although qualitative, does show a strong agreement between the two sources, for current speed and direction. The statistical comparisons showed varying degrees of agreement between the observations and model results. Correlations were computed on the 2016 observational data and model results at 50, 250, 550, and 750 m showing a decrease in from the surface (~0.93 at 50 m) to bottom (~0.80 at 750 m). An EOF analysis was performed to investigate the presence of the flow features in the dominant mode one. This revealed little information on the quality of the model that was not observable in the model-observation comparison figures.

Ocean Response to Tropical Storm Forcing.

Two hurricanes, Hurricane Barry, and Hurricane Laura passed not far from the current measurement site, ID 42369. The tracks of these hurricanes and associated wind speed were obtained from the NOAA IBTrACS dataset and are shown in Figure 6 along with the location of the measurement site.

Hurricane Barry began in the Midwest as a trough of low pressure on July 6th, 2019, and drifted south into the Gulf of Mexico, becoming a tropical storm by July 11th. As the storm moved westward, it experienced northerly wind shear, intensifying the conditions and was upgraded to a hurricane on the morning of July 13th. Hurricane Barry passed within 80km of MD while it was classified as a tropical storm on July 12th with wind speeds of 23.15m/s.

Hurricane Laura originated off the west coast of Africa on August 16th, 2020, which traveled west and developed into a tropical depression on August 19th. Tropical Storm Laura continued northwestward, crossing Cuba on August 24th and entered the GOM and became a hurricane on August 25th. Laura explosively intensified to category 4 on August 26th with peak intensity of 67m/s and a minimum central pressure of 937millibars. Laura traveled within an 88km radius of MD as a category 4 storm with wind speeds of 67m/s.

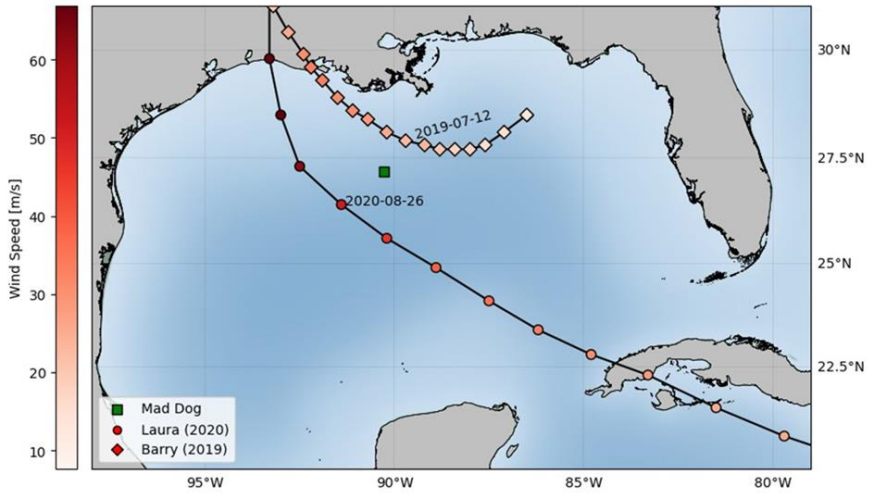

Figure 6. Hurricane Laura and Hurricane Barry's paths through the Gulf of Mexico, nearby station ID 42369 (MD).

To evaluate the model performance on representing the ocean response to Hurricane Barry and Hurricane Laura, model and observational data from July 1-31st, 2019 and August 20-September 10th, 2020, were compared at MD, respectively. These comparisons were made both statistically and visually.

MD ADCP data, in the month of July (Figure 7), show an increase in the north velocity in the upper 400m of the water column after Hurricane Barry began to weaken. This increase in velocity at the surface is seen in both models, but the timing of the increase is delayed in both the 1/100° and 1/25° resolution models. The 1/25° resolution model velocity increase extends deeper than what is resolved in the 1/100° resolution model and better represents what was observed at MD. Additionally, there are 'stripes' of higher/lower velocities extending deep into the water column creating a striated pattern in all data (observed and models). These are signatures of near-inertial oscillations, which the temporal and spatial variability, in the upper ocean, is dependent on variations in wind forcing. High frequency current variability in the deep water is dominated by near-inertial oscillations, some generated by hurricanes travelling across the GOM, propagating vertically down to the seafloor. Both resolution models resolve these vertical propagations.

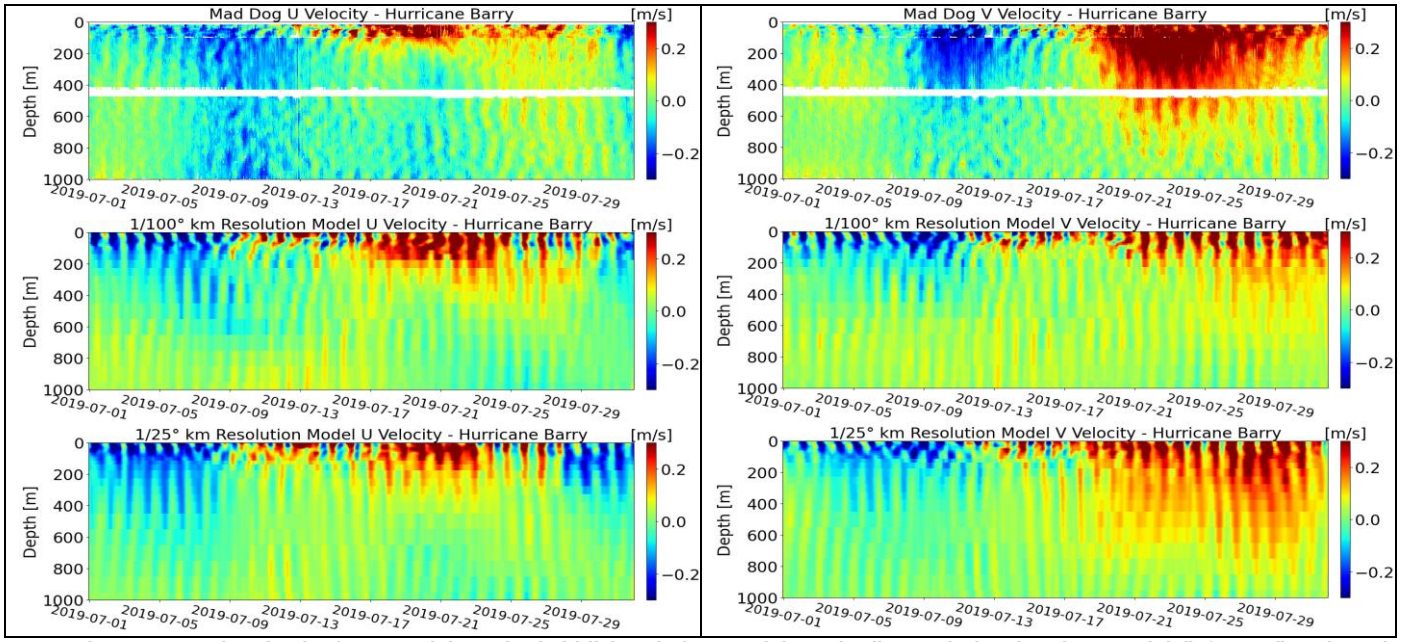

Figure 7. Mad Dog ADCP data (top), 1/100° model results (middle) and 1/25° model results (bottom) showing the East (U) (left panel) and North (V) (right panel) velocity components during Hurricane Barry (2019).

For a statistical comparison, the correlation on the observations and model results at 20m were computed. The correlation coefficients of East and North velocity at 20m for the 1/25° resolution model were 0.64, and 0.67. For the higher resolution model (1/100°), the R values were 0.71 and 0.64 for East and North velocities.

Data from August 20th – September 10th, 2020, also showed an increase in velocities in the upper 100m with pulses of higher values from August 26 through September 1st, coinciding with the time that Hurricane Laura was passing by (Figure 8). The timing of these pulses in both resolutions of the model match well with the observed pulses. Similar to the July 2019 case, vertical 'stripes' of higher velocities are seen extending throughout the water column. The 'stripes' are slanted reflecting the upward phase propagation (downward energy propagation) of the oscillations, the phenomenon well-resolved by the models.

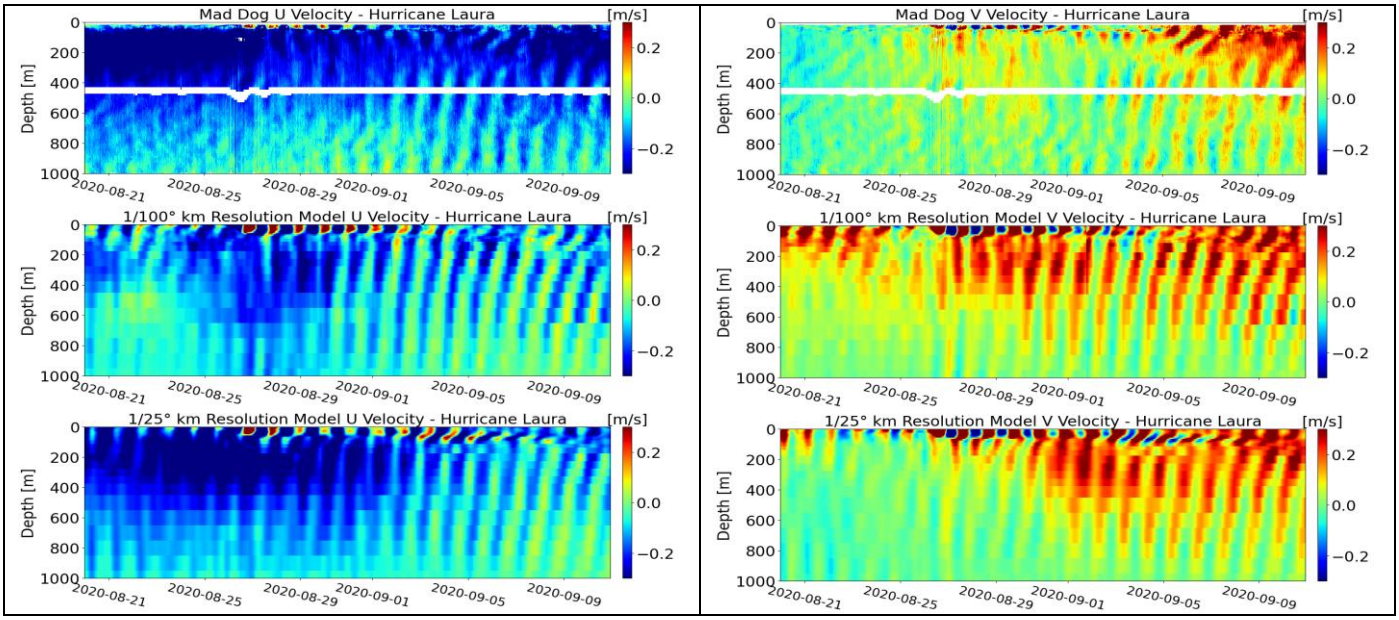

Figure 8. Mad Dog ADCP data (top), 1/100° model results (middle) and 1/25° model results (bottom) showing the East (U) (left panel) and North (V) (right panel) velocity component during Hurricane Laura (2020).

Morlet's wavelet analysis showed that the occurrence of amplitude peaks in the models generally agreed with the occurrence of amplitude peaks in the observational data. The major difference between the model and measurements is the more continuous presence of near-initial oscillations in the reanalysis data. While the measurements show separate trains of oscillations at the inertial period, each associated with a wind event, such as the passage of the storm, the model show the presence of near-initial oscillation, practically, at any time, with increase in the amplitude after a wind event.

Discussion and Summary

The detailed results of model-to-observations analyses revealed that, for the most energetic events, such as LCE, the cases that were selected for model-to-observations comparison showed good agreement between model and observations. In particular, (i) peak current speeds in the model and in the observations occur approximately at the same time, (ii) peak current magnitudes in the model datasets and in the observations are the same, approximately, (iii) penetration of the strong currents into sub-surface layers is almost the same in model and observational data, and (iv) the evolution of current direction is similar in model data and observations.

For sub-surface flow events, the match between model and observations is not as good as for the LCE flows. However, it is important that the model, especially the 1km resolution data, resolve such phenomena to some extent and, for approximately 40% of the selected cases, model output and observations agree in a qualitative manner. An EOF analysis was performed to investigate the presence of the flow features in the dominant mode. This revealed little information on the quality of the model that was not observable in the model-observation comparison figures. Qualitatively, the model with 1km resolution shows a slightly better match with observations compared to the 4km resolution output for the selected cases of the subsurface flows.

As a part of the process-oriented analysis, model data helped identify the area of origin of the most prominent subsurface eddy observed at several sites in October 2016. That cyclonic eddy was generated in March 2016 as a friction eddy between the western slope of DeSoto Canyon and the northern boundary of the LC. The eddy was quasi-stationary through September 2016, then propagated towards the west along the bathymetry contours, reaching the area of Green Canyon, where measurements were collected, by October 2016.

During different events, both the 1km and 4km resolution models vary on their ability to resolve the flow. To quantify how the models perform, Willmott's refined index of model performance was determined for selected events. According to the refined index, the model results compare well with the observational data. The index values indicate that the sum of the error-magnitudes is approximately 1/3 of the sum of the perfect-model-deviation and observed-deviation magnitudes. For the fine resolution and coarser resolution model reanalyses, the Willmott's refined index values are close in magnitude.

To evaluate the model performance on representing the ocean response to tropical storms, model and observational data from July 1-31st, 2019 (Hurricane Barry) and August 20-September 10th, 2020 (Hurricane Laura), were compared to measurements collected at the Mad Dog mooring site. These comparisons were made both statistically and visually. Mad Dog ADCP data, in the month of July, show an increase in the north velocity in the upper 400m of the water column after Hurricane Barry began to weaken. This increase in velocity at the surface is seen in both models, but the timing of the increase is delayed in both the 1/100° and 1/25° resolution models. The 1/25° resolution model velocity increase extends deeper than what is resolved in the 1/100° resolution model and better represents what was observed. Additionally, observations and models show similar signatures of near-inertial oscillations that developed in the wake of the storms**.**

Acknowledgements

The authors acknowledge the support from the Bureau of Ocean Energy Management under award number M20AC10020-40, the Gulf Research Program of the National Academies of Sciences, Engineering, and Medicine under award number 2000013149, and the Office of Naval Research under grant number N00014-19-1-2671. The content is solely the responsibility of the authors and does not necessarily represent the official views of the Bureau of Ocean Energy Management, the Gulf Research Program, the National Academies of Sciences, Engineering, and Medicine, and the Office of Naval Research.

References

Cooper, M., & Haines, K. (1996). Altimetric assimilation with water property conservation. *Journal of Geophysical Research*, *101*, 1059–1077. Retrieved from https://api.semanticscholar.org/CorpusID:129918767.

Dorandeu, J., & Le Traon, P. Y. (1998). *Effects of Global Mean Atmospheric Pressure Variations on Mean Sea Level Changes from TOPEX/Poseidon*.

Egbert, G. D., & Erofeeva, S. Y. (2002). *Efficient Inverse Modeling of Barotropic Ocean Tides*.

Evensen, G. (2003). The Ensemble Kalman Filter: theoretical formulation and practical implementation. *Ocean Dynamics*, *53*(4), 343–367. https://doi.org/10.1007/s10236-003-0036-9

Hamilton, P. (1990). Deep Currents in the Gulf of Mexico. *Journal of Physical Oceanography*, *20*, 1087–1104.

Hamilton, P., & Badan, A. (2009). Subsurface jets in the northwestern Gulf of Mexico. *Journal of Physical Oceanography*, *39*(11), 2875–2891. https://doi.org/10.1175/2009JPO4158.1

Ivanov, L., Ramos, R., Sharma, N., Magnell, B., Tran, M., Storie, J., et al. (2018). Deep Sub-Surface Eddies in the Gulf of Mexico. In *OCEANS 2018 MTS/IEEE Charleston* (pp. 1–9). https://doi.org/10.1109/OCEANS.2018.8604876

Lewis, J. K., Kirwan, A. D., & Forristall, G. Z. (1989). Evolution of a warm-core ring in the Gulf of Mexico: Lagrangian observations. *Journal of Geophysical Research: Oceans*, *94*(C6), 8163–8178. https://doi.org/10.1029/jc094ic06p08163

Magnell, B. A., & Ivanov, L. (2014). Signatures of Mid-Water "Jets" in the Gulf Of Mexico BOEM NTL Dataset. In *OTC 25421* (pp. 5–8).

Oey, L. Y., & Zhang, H. C. (2004). The generation of subsurface cyclones and jets through eddy-slope interaction. *Continental Shelf Research*, *24*(18), 2109–2131. https://doi.org/10.1016/j.csr.2004.07.007

Oke, P. R., Allen, J. S., Miller, R. N., Egbert, G. D., & Kosro, P. M. (2002). Assimilation of surface velocity data into a primitive equation coastal ocean model. *Journal of Geophysical Research: Oceans*, *107*(9). https://doi.org/10.1029/2000jc000511

Schreck, C., & National Center for Atmospheric Research Staff (Eds.). (2022, September 9). The Climate Data Guide: IBTrACS: Tropical cyclone best track data. Retrieved January 22, 2024, from https://climatedataguide.ucar.edu/climate-data/ibtracs-tropical-cyclone-best-track-data on 2024-01-23.

Srinivasan, A., Chin, T. M., Chassignet, E. P., Iskandarani, M., & Groves, N. (2022). A Statistical Interpolation Code for Ocean Analysis and Forecasting. *Journal of Atmospheric and Oceanic Technology*, *39*(3), 367–386. https://doi.org/10.1175/JTECH-D-21-0033.1

DiMarco, S. F., Howard, M. K., Nowlin Jr., W. D., & Reid, R. O. (2004). *Subsurface, High-Speed Current Jets in the Deepwater Region of the Gulf of Mexico Final Report New Orleans*.

Storie, J., Ramos, R., Leber, M., Nowak, H., Young, M., & Magnell, B. (2023). Evaluation of Loop Current/ Loop Current Eddy Fronts to Guide Offshore Oil & Gas Operations. In *Offshore Technology Conference*. https://doi.org/https://doi.org/10.4043/32643-MS

Le Traon, P. Y., & Ogor, F. (1998). ERS-1/2 orbit improvement using TOPEX/POSEIDON: The 2 cm challenge. *Journal of Geophysical Research: Oceans*, *103*(3334), 8045–8057. https://doi.org/10.1029/97jc01917

Velissariou, P. (2014). Gulf of Mexico High-Resolution (0.01° x 0.01°) Bathymetric Grid - Version 2.0. Gulf of Mexico Research Initiative Information and Data Cooperative (GRIIDC), Harte Research Institute, Texas A&M University–Corpus Christi.

Vukovich, F. M., & Crissman, B. W. (1986). Aspects of warm rings in Gulf of Mexico. *Journal of Geophysical Research*, *91*(C2), 2645–2660. https://doi.org/10.1029/JC091iC02p02645

Vukovich, Fred M., & Maul, G. A. (1985). Cyclonic Eddies in the Eastern Gulf of Mexico. *Journal of Physical Oceanography*, *15*, 105–117.